Astronomy & Astrophysics manuscript no. output
September 1, 2025

Non-equilibrium thermodynamics with dust and gas in protoplanetary disks

Nadine H. Soliman[1,2], Leonardo Krapp[3], and Andrew N. Youdin[4]

[1] Institute for Advanced Study, Einstein Drive, Princeton, NJ 08540, USA;e-mail: `nsoliman@ias.edu`
[2] TAPIR, Mailcode 350-17, California Institute of Technology, Pasadena, CA 91125, USA
[3] Departamento de Astronomía, Facultad de Ciencias Físicas y Matemáticas Universidad de Concepción, Av. Esteban Iturra s/n Barrio Universitario, Casilla 160-C. Chile
[4] Department of Astronomy and Steward Observatory, University of Arizona, Tucson, AZ 85721, USA.

Received XXXX; accepted XXXX

ABSTRACT

Context. The evolution of protoplanetary disks and the formation of planets are strongly influenced by turbulence and vortices, often driven by hydrodynamic instabilities. Among these, the vertical shear instability (VSI) is especially important, but its growth depends critically on rapid cooling, making it highly sensitive to the disk's thermodynamic properties. Since local cooling rates are often dominated by the thermal coupling between dust and gas, dust thermal accommodation becomes a key factor in determining whether the VSI can operate.

Aims. We aim to quantify the conditions that allow the VSI to develop by self-consistently computing disk cooling times, accounting for both a realistic grain size distribution and non-equilibrium energy exchange between gas and dust.

Methods. We develop an unconditionally stable, first-order implicit scheme for solving the coupled thermal evolution of gas and dust components in the non-equilibrium regime. Our method is applicable across a wide range of densities, temperatures, and grain sizes relevant to protoplanetary disks.

Results. We validate the scheme through a suite of tests that demonstrate its accuracy, stability, and convergence. We then apply the method to two-dimensional hydrodynamical simulations of axisymmetric protoplanetary disks to investigate how dust-gas thermal interactions regulate the onset and growth of the VSI.

Key words.

1. Introduction

Protoplanetary disks host a variety of hydrodynamic instabilities that play a central role in their evolution. These instabilities generate turbulence, transport angular momentum, and produce vortices and other coherent structures that can concentrate solids and promote planetesimal formation (Youdin & Lithwick 2007; Chiang & Youdin 2010; Armitage 2011; Lyra & Umurhan 2019). Among these, the Vertical Shear Instability (VSI) has received particular attention as a robust hydrodynamic source of turbulence in the outer disk (Urpin & Brandenburg 1998; Urpin 2003; Lesur et al. 2023).

The VSI is triggered by vertical gradients in orbital velocity, which produce vertical shear and induce vertical motions within the disk (Nelson et al. 2013; Stoll & Kley 2014). For the VSI to grow, these motions must overcome stabilizing buoyancy forces, which requires rapid thermal relaxation, i.e., cooling times much shorter than the local dynamical timescale (Goldreich & Schubert 1967; Lin & Youdin 2015; Manger et al. 2021). If cooling is too slow, buoyancy suppresses perturbations, preventing the instability from developing.

Cooling within the disk is governed by a combination of radiative transfer and collisional energy exchange between gas and solids. In most regions, dust grains dominate this process due to their high infrared emissivity, which allows them to radiate thermal energy far more efficiently than the gas (Chiang & Goldreich 1997; Malygin et al. 2017; Barranco et al. 2018). Gas cools indirectly through collisions with dust in a process known as thermal accommodation, whereby energy is transferred from the hotter component to the cooler one. The heat absorbed by the dust is then radiated away in the infrared. Many global disk models assume that this exchange is sufficiently rapid to maintain local thermal equilibrium (LTE) between gas and dust, thereby justifying the use of isothermal or near-isothermal approximations, common in global simulations of the VSI (Stoll & Kley 2014; Barker & Latter 2015).

However, LTE is not guaranteed. The gas–dust coupling timescale depends on gas density, dust density, grain size distribution, and temperature differences between phases (Burke & Hollenbach 1983; Draine 2011). In low-density regions, or when large grains dominate, collisional coupling can be slow compared to dynamical timescales, leading to significant temperature differences between gas and dust (Thi et al. 2019). Because the growth of many disk instabilities, including the VSI, is highly sensitive to the cooling rate, neglecting non-equilibrium thermodynamics can qualitatively alter predictions for their growth and saturation amplitudes.

The problem is further complicated by the fact that protoplanetary disks contain a broad and evolving distribution of grain sizes, shaped by coagulation, fragmentation, radial drift, and vertical settling (Birnstiel et al. 2012). This dust evolution alters both the spatial distribution and local abundance of grains of different sizes which can leading to strong radial and vertical gradients in cooling efficiency. Cooling efficiency depends sensitively on grain size: sub–micron grains remain tightly coupled to the gas and equilibrate thermally on very short timescales, while millimeter- to centimeter-sized grains can remain thermally decoupled over many dynamical times. A single-size dust approximation therefore fails to capture the spatially and temporally varying cooling rates associated with realistic size distributions and their dynamics. Multi-size treatments are required to model where and how instabilities like the VSI can operate, and to assess their implications for dust concentration and planetesimal formation

However, fully evolving the coupled dust and gas energy equations under non-equilibrium conditions remains numerically challenging. The thermal exchange terms are stiff: in dense regions of the disk, cooling times can be many orders of magnitude shorter than the orbital period. Explicit timestepping schemes are therefore unstable unless prohibitively small time steps are used. While implicit methods avoid this limitation, conventional implementations typically require solving large matrix systems, with computational cost scaling poorly with the number of dust species. This has limited most global simulations of the VSI to simplified thermodynamic treatments. Most models either assume instantaneous dust–gas thermal equilibrium (LTE) or adopt a prescribed β–cooling model, where the cooling time is parameterized as a fixed fraction of the local dynamical time (Pfeil & Klahr 2021; Lin & Youdin 2015; Nelson et al. 2013). Although these models can provide physical insight and can be calibrated to match disk conditions, they do not capture the full nonlinear evolution of energy exchange processes.

In this work, we present a new method for modeling dust–gas thermal interactions in protoplanetary disks. We implement a first-order implicit scheme for evolving the thermal energy of both the gas and a discretized dust grain size distribution within the GPU code FARGO3D (Benítez-Llambay & Masset 2016). The scheme is unconditionally stable, avoids costly matrix inversions, and scales linearly with the number of dust species, making it well-suited for computationally demanding global disk simulations. We validate the method against analytic solutions and apply it to study the impact of dust–gas thermal decoupling on the linear growth and nonlinear saturation of the VSI in protoplanetary disks.

This report is organized as follows. In Section 2, we describe our numerical methods, including the implementation of an implicit integrator for the internal energy equations that captures the effects of thermal accommodation. In Section 3, we present a set of benchmark problems: nonlinear two-fluid thermal relaxation and the propagation of sound waves in the presence of thermal accommodation and drag forces. In Section 4, we extend the framework to include dust radiative cooling, outlining both an operator-splitting approach and a combined implicit scheme that simultaneously treats collisional and radiative processes. In Section 5, we apply these methods to simulations of the VSI and highlight the impact of dust–gas thermodynamics on the instability's growth. Finally, in Section 6, we summarize our findings and discuss their implications.

2. Numerical Methods

Consider a one-dimensional system composed of a dusty fluid, consisting of gas and $N-1$ distinct dust species. Each dust species i is characterized by a grain radius $a_{d,i}$, mass density $\rho_{d,i}$, temperature $T_{d,i}$, and a constant-volume specific heat capacity $c_{d,i}$. The grains are assumed to be made of the same material, with a shared intrinsic (material) density ρ_s. For simplicity, we assume the specific heat is identical for all species, such that $c_{d,i} = c_d$ for all i.

The gas component is described by its mass density ρ_g, temperature T_g, mean molecular mass $\bar{m}_g$, and constant-volume specific heat capacity c_g.

The internal energy exchange between the gas and each dust species occurs through collisions and radiative cooling. The energy balance equations are:

$$\rho_g c_g \frac{dT_g}{dt} = -\Lambda_g, \tag{1}$$

$$\rho_{d,i} c_d \frac{dT_{d,i}}{dt} = \Lambda_{d,i} - \Gamma_{d,i}, \tag{2}$$

$$\Lambda_g = \sum_{k=1}^{N-1} \Lambda_{d,i}, \tag{3}$$

$$\Lambda_{d,i} = \pi a_{d,i}^2 n(a_{d,i}) n_g \bar{v}_g (2\mathscr{A}) k_B (T_g - T_d), \tag{4}$$

$$\Gamma_{d,i} = 4\pi a_{d,i}^2 n(a_{d,i}) Q(a_{d,i}, T_{d,i}) \sigma_{SB} (T_{d,i}^4 - T_{eq}^4) \tag{5}$$

where Λ_g and $\Lambda_{d,i}$ represent the collisional energy transfer rate for the gas and dust species i, respectively. The grain number density is given by $n(a_{d,i}) = 3\rho_{d,i}/(4\pi\rho_s a_{d,i}^3)$, the mean thermal velocity of the gas by $\bar{v}_g \sim \sqrt{2k_B T_g/\bar{m}_g}$, and the radiative efficiency factor by $Q(a_{d,i}, T_{d,i}) = \min(2\pi a_{i,d}/\lambda_{d,i}, 1)$, where $\lambda_{d,i} = hc/(4k_B T_{d,i})$. To cast this system in matrix form, we define the temperature vector $\mathbf{T} = (T_g, T_{d,1}, T_{d,2}, \ldots, T_{d,N-1})$, and radiative dust cooling term $\mathbf{\Gamma} = (0, \Gamma_{d,1}, \Gamma_{d,2}, \ldots, \Gamma_{d,N-1})$ and obtain

$$\frac{d\mathbf{T}}{dt} = \mathbf{MT} + \mathbf{\Gamma}, \tag{6}$$

where the energy exchange matrix $\mathbf{M}$ an $N \times N$ matrix given by

$$\mathbf{M} = \begin{pmatrix} -\tilde{\boldsymbol{\epsilon}}_{\boldsymbol{i}} \cdot \boldsymbol{\alpha} & \tilde{\boldsymbol{\epsilon}}^{\mathbf{0}} \boldsymbol{\alpha}^T \\ \boldsymbol{\alpha}^T & -\mathrm{diag}(\boldsymbol{\alpha}) \end{pmatrix}, \tag{7}$$

and the relevant vectors are defined as $\tilde{\epsilon}_i = c_{dg}\epsilon_i$, $\tilde{\boldsymbol{\epsilon}}^0 = (\tilde{\epsilon}_1^0, \tilde{\epsilon}_2^0, \ldots, \tilde{\epsilon}_{N-1}^0)$, $\boldsymbol{\alpha} = (\alpha_1, \alpha_2, \ldots, \alpha_{N-1})$, and the collisional coupling coefficients are given by

$$\alpha_i \equiv \frac{3(k_B/\bar{m})^{3/2} T_g^{1/2} \rho_g}{4\rho_s c_d a_{d,i}}. \tag{8}$$

Let us first consider the simplest thermal coupling scenario between dust and gas where the only relevant processes governing the internal energy exchange between the gas and each dust species occurs through collisions and ignoring dust radiative cooling, i.e. $\Gamma_{d,i} = 0$.

Let $\mathbf{T}^{n+1}$ denote the numerical approximation to the solution of the equations at $t^{n+1} = t^n + \Delta t$. For this simplified case a fully implicit first-order scheme is obtained by solving the following system:

$$(\mathbf{I} - \Delta t\mathbf{M}) T^{n+1} = T^n. \tag{9}$$

Expanding this yields:

$$\begin{cases} (1 + c_{dg} \sum\limits_{k=1}^{N-1} \epsilon_k^n \alpha_k^n \Delta t)\, T_g^{n+1} - c_{dg} \sum\limits_{k=1}^{N-1} \epsilon_k^n \alpha_k^n \Delta t\, T_{d,k}^{n+1} = T_g^n, \\ -\alpha_i^n \Delta t\, T_g^{n+1} + (1 + \alpha_i^n \Delta t)\, T_{d,i}^{n+1} = T_{d,i}^n, \forall\, 1 \le i \le N-1. \end{cases} \tag{10}$$

To derive the closed-form solution at timestep $n+1$, we introduce the effective pressure p^n and effective density ρ^n at timestep n, defined as:

$$p^n = \rho_g^n T_g^n + c_{p,dg} \sum_{k=1}^{N-1} \frac{\alpha_k^n \Delta t}{1 + \alpha_k^n \Delta t} \rho_{d,k}^n T_{d,k}^n, \tag{11}$$

$$\rho^n = \rho_g^n + c_{p,dg} \sum_{k=1}^{N-1} \frac{\alpha_k^n \Delta t}{1 + \alpha_k^n \Delta t} \rho_{d,k}^n. \tag{12}$$

Substituting into the discretized system yields the closed-form expressions for the updated temperatures:

$$T_g^{n+1} = p^n / \rho^n, \tag{13}$$

$$T_{d,i}^{n+1} = \frac{T_{d,i}^n}{1 + \alpha_i^n \Delta t} + \left(\frac{\alpha_i^n \Delta t}{1 + \alpha_i^n \Delta t} \right) \frac{p^n}{\rho^n}. \tag{14}$$

2.1. *Effective relaxation time*

Although the implicit scheme is formally unconditionally stable, its accuracy is not guaranteed for arbitrarily large timesteps Δt. To quantify this behavior, we examine the effective cooling rate associated with the relaxation of gas temperature perturbations toward the dust equilibrium temperature T_d. Assuming the dust remains fixed at equilibrium (e.g., due to its rapid radiative cooling), the numerical solution can be expressed as an exponential relaxation

$$T_g(t) = T_d + (T_g^0 - T_d) e^{-\alpha_{\rm eff} t}, \tag{15}$$

with an effective damping rate $\alpha_{\rm eff}$.

This effective relaxation rate of the first order implicit scheme can be estimated by considering the deviation from equilibrium of the gas temperature as

$$T_g^{n+1} - T_d = \frac{T_g^n + \dfrac{\tilde\epsilon\,\alpha\Delta t}{1 + \alpha\Delta t} T_d}{1 + \dfrac{\tilde\epsilon\,\alpha\Delta t}{1 + \alpha\Delta t}} - T_d. \tag{16}$$

Thus, the amplification factor between successive steps satisfies

$$e^{-\alpha_{\rm eff}\Delta t} = \frac{T_g^{n+1} - T_d}{T_g^n - T_d}, \tag{17}$$

which yields

$$\alpha_{\rm eff} = \frac{1}{\Delta t} \log\left(\frac{1 + (1 + \tilde\epsilon)\alpha\Delta t}{1 + \alpha\Delta t} \right). \tag{18}$$

Several limiting regimes are worth noting:

- For small timesteps ($\alpha\Delta t \ll 1$), the numerical solution recovers the physical cooling rate, $\alpha_{\rm eff} \approx \tilde\epsilon\alpha$.
- For intermediate timesteps ($\alpha\Delta t \sim 1$) and $\tilde\epsilon \ll 1$, the effective rate is suppressed,

  $$\alpha_{\rm eff} \simeq \frac{\tilde\epsilon\,\alpha}{1 + \alpha\Delta t}, \tag{19}$$

  i.e. relaxation is artificially slowed by a factor $(1 + \alpha\Delta t)^{-1}$.
- In the stiff regime ($\alpha\Delta t \gg 1$), the effective rate vanishes, $\alpha_{\rm eff} \to 0$, and the gas behaves adiabatically.

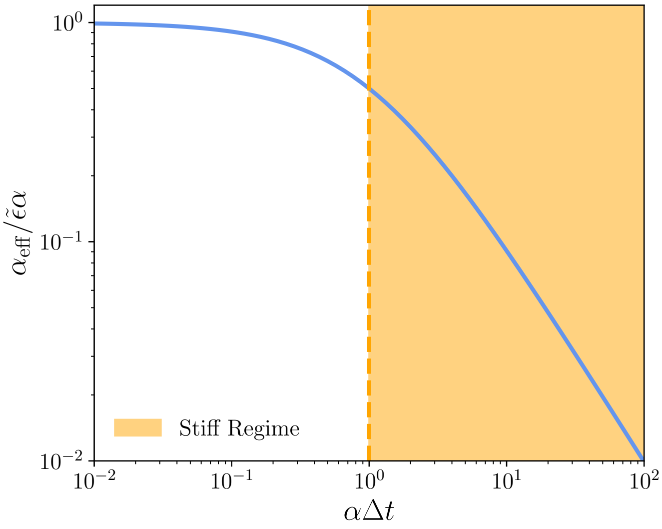

Fig. 1. Ratio of the effective cooling rate $\alpha_{\rm eff}$ to the physical rate α as a function of the dimensionless timestep $\alpha\Delta t$. The plot illustrates that, although the implicit scheme is unconditionally stable, accurate recovery of the physical cooling requires $\alpha\Delta t \ll 1$. For larger timesteps, the scheme can underestimate the cooling rate by several orders of magnitude.

These regimes are summarized in Fig. 1, which displays the ratio $\alpha_{\rm eff}/\alpha$ as a function of $\alpha\Delta t$. While the implicit scheme is formally unconditionally stable, accurately capturing the physical relaxation requires resolving the dust cooling timescale, i.e., ensuring $\alpha\Delta t \ll 1$. If this condition is not met, the numerical scheme systematically underestimates the cooling rates.

3. Numerical Tests

This section describes the tests conducted to evaluate the accuracy, convergence, and robustness of the numerical method and implementation outlined in Section 2.

3.1. *Non-linear two-fluid relaxation*

As an initial validation of our implementation, we consider the thermal relaxation of gas and dust toward a common equilibrium temperature via dust–gas energy exchange. Assuming constant and uniform densities for both components, the system reduces to a pair of coupled, nonlinear ordinary differential equations governing the temperature evolution:

$$\rho_g c_g \frac{dT_g}{dt} = -\tilde\Lambda_0 \sqrt{T_g} (T_g - T_d)\,, \tag{20}$$

$$\rho_d c_d \frac{dT_d}{dt} = \tilde\Lambda_0 \sqrt{T_g} (T_g - T_d)\,, \tag{21}$$

where $\tilde\Lambda_0$ is a constant independent of gas and dust temperature. Conservation of total energy ε_0 implies

$$c_g \rho_g T_g(t) + c_d \rho_d T_d(t) = c_g \rho_g T_g(0) + c_d \rho_d T_d(0) = \varepsilon_0. \tag{22}$$

The system therefore asymptotically relaxes to a common equilibrium temperature,

$$T_\infty = \frac{\rho_g c_g T_g(0) + \rho_d c_d T_d(0)}{\rho_g c_g + \rho_d c_d}, \tag{23}$$

Using energy conservation, the governing equations can be reduced to a single nonlinear ODE for $T_g(t)$ that admits a closed-form solution:

$$\frac{dT_g}{dt} = -\frac{\tilde{\Lambda}_0}{c_g\rho_g c_d\rho_d}\sqrt{T_g}(T_g(c_d\rho_d + c_g\rho_g) - \varepsilon_0). \tag{24}$$

$$\tag{25}$$

We then obtain the solution for $T_g(t)$,

$$T_g(t) = \begin{cases} T_\infty \frac{\eta e^x - 1}{\eta e^x + 1}, & \frac{T_g^0}{T_\infty} < 1 \\ T_\infty \frac{\eta e^x + 1}{1 - \eta e^x}, & \frac{T_g^0}{T_\infty} > 1 \end{cases} \tag{26}$$

$$\eta = \begin{cases} \frac{1+\sqrt{T_g^0/T_\infty}}{1-\sqrt{T_g^0/T_\infty}}, & \frac{T_g^0}{T_\infty} < 1 \\ \frac{1+\sqrt{T_g^0/T_\infty}}{\sqrt{T_g^0/T_\infty}-1}, & \frac{T_g^0}{T_\infty} > 1 \end{cases} \tag{27}$$

$$x = \frac{\tilde{\Lambda}_0 t}{c_d\rho_d c_g\rho_g}\sqrt{\varepsilon_0(c_g\rho_g + c_d\rho_d)}, \tag{28}$$

$$\tag{29}$$

To validate our numerical scheme, we initialize the system with $T_g(t = 0) = 5\,T_d(t = 0)$ and a cooling rate $\alpha = 1$, and evolve the equations using our implicit integration method. The numerical solution is compared to the analytical solution, and the error is quantified using the maximum norm. As shown in Fig. 2, the numerical solution closely follows the analytical solution. Repeating the test across a range of timesteps confirms that the numerical error scales linearly with Δt up to $\alpha\Delta t \sim 1$ as shown in Fig. 3, consistent with the first-order accuracy expected from the implicit Euler method. We consider $\alpha\Delta t \gg 1$ to highlight the stiff regime, in which the effective relaxation rate deviates from the physical rate. These results demonstrate that the implementation accurately captures the relaxation dynamics and converges systematically to the analytical solution, provided that timesteps are chosen appropriately.

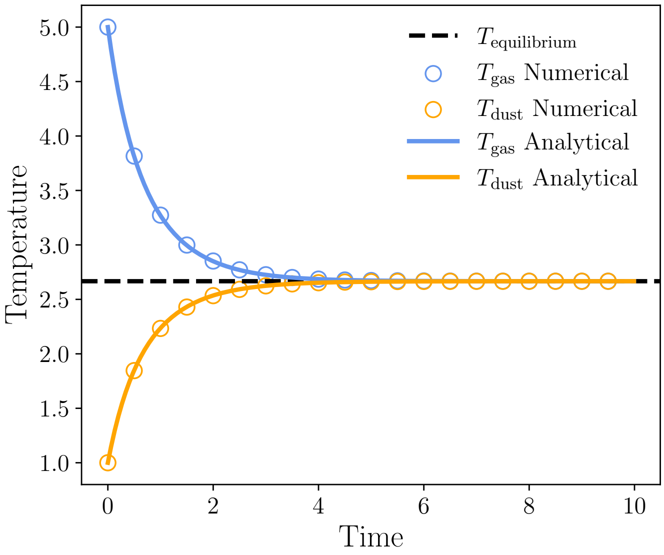

Fig. 2. Temperature evolution of a two-fluid system consisting of gas and dust components coupled via collisional cooling. The numerical solution (solid lines) is compared to the analytical solution (circles), demonstrating close agreement. The system converges to the expected equilibrium state.

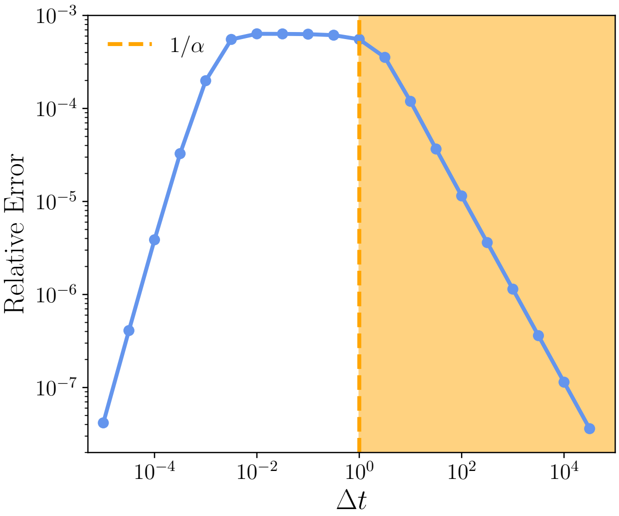

Fig. 3. Maximum-norm error of the numerical solution as a function of timestep Δt. The linear scaling of the error up to $\alpha\Delta t \sim 1$ (dashed line) confirms first-order convergence of the implicit Euler method and highlights the stiff regime (highlighted), where the effective relaxation rate underestimates the physical rate

3.2. Sound waves with thermal accommodation and drag force

We next couple the hydrodynamics with our thermal accommodation module. This extends the multifluid sound-wave test of Benítez-Llambay et al. (2019) by including collisional energy exchange between gas and dust in addition to the usual aerodynamic drag. The problem setup consists of a uniform medium initially at rest, with dust and gas in thermal equilibrium. The dust is represented by a size distribution of $N - 1$ species, each characterized by a stopping time $t_{s,i}$ and an initial dust-to-gas mass ratio ϵ_i^0. The corresponding linearized fluid equations are

$$\partial_t\delta\rho_g + \rho_g^0\partial_x\delta v_g = 0, \tag{30}$$

$$\partial_t\delta\rho_{d,i} + \rho_{d,i}^0\partial_x\delta v_{d,i} = 0, \tag{31}$$

$$\partial_t\delta v_g + \sum_{i=1}^{N}\frac{\epsilon_i^0}{t_{s,i}}(\delta v_g - \delta v_{d,i}) + \frac{1}{\rho_g^0}\partial_x\delta P = 0, \tag{32}$$

$$\partial_t\delta v_{d,i} - \frac{1}{t_{s,i}}(\delta v_g - \delta v_{d,i}) = 0, \tag{33}$$

$$\partial_t T_g + (\gamma - 1)T_g^0\partial_x\delta v_g + \sum_{i=1}^{N}\frac{\Lambda_{0,i}(T_g^0)}{c_g\rho_g^0}(\delta T_g - \delta T_{d,i}) = 0, \tag{34}$$

$$\partial_t T_{d,i} - \frac{\Lambda_{0,i}(T_g^0)}{c_d\rho_{d,i}^0}(\delta T_g - \delta T_{d,i}) = 0. \tag{35}$$

In the isothermal limit, the dispersion relation of the system of equations reveals two damped propagating waves and N-2 purely damped modes.

3.3. No drag force case

First let us consider the simple case where the dust does not experience drag or exert a back-reaction force, and only acts as a coolant. In this simplified case the relevant linearized equations are

$$\partial_t \delta\rho_g + \rho_g^0 \partial_x \delta v_g = 0, \tag{36}$$

$$\partial_t \delta v_g + \frac{1}{\rho_g^0} \partial_x \delta P = 0, \tag{37}$$

$$\partial_t \delta T_g + (\gamma - 1) T_g^0 \partial_x \delta v_g + \sum_{i=1}^{N} \frac{\Lambda_{0,i}(T_g^0)}{c_g \rho_g^0} (\delta T_g - \delta T_{d,i}) = 0, \tag{38}$$

$$\partial_t \delta T_{d,i} - \frac{\Lambda_{0,i}(T_g^0)}{c_d \rho_{d,i}^0} (\delta T_g - \delta T_{d,i}) = 0. \tag{39}$$

Assuming linear perturbations of the form $\delta f = \tilde{\delta f} e^{ikx - iwt}$ and normalizing temperature perturbation by T_g^0, velocity perturbations by c_s, and density perturbation by ρ_g^0, we obtain

$$-i\omega \delta\tilde{\rho}_g = -i\omega_s \delta\tilde{v}_g, \tag{40}$$

$$-i\omega \delta\tilde{v}_g = -\frac{\omega_s}{\gamma} \left(\delta\tilde{T}_g + \delta\tilde{\rho}_g \right), \tag{41}$$

$$-i\omega \delta\tilde{T}_g = -i(\gamma - 1)\omega_s \delta\tilde{v}_g - \sum_{k=1}^{N-1} \tilde{\epsilon}_k^0 \alpha_k (\delta\tilde{T}_g - \delta\tilde{T}_{d,k}), \tag{42}$$

$$-i\omega \delta\tilde{T}_{d,i} = \alpha_i (\delta\tilde{T}_g - \delta\tilde{T}_{d,i}), \tag{43}$$

where $\delta P/P^0 = \delta\rho_g/\rho_g^0 + \delta T_g/T_g^0$, and $\omega_s = kc_s$, $\alpha_i = \frac{\Lambda_{0,i}(T_g^0)}{c_d \rho_{d,i}^0}$, and noting that $c_s^2 = \gamma R_\mu T_g^0$.

This system of equations can be written in matrix form as $\mathbf{M}\tilde{\delta} = -i\omega\tilde{\delta}$, where the perturbation vector $\tilde{\delta} = (\delta\tilde{\rho}_g, \delta\tilde{v}_g, \delta\tilde{T}_g, \delta\tilde{T}_{d,1}, \delta\tilde{T}_{d,2}, \ldots, \delta\tilde{T}_{d,N-1})$ and $\mathbf{M}$ is an $(N+2) \times (N+2)$ matrix

$$\mathbf{M} = \begin{pmatrix} 0 & -i\omega_s & 0 & \mathbf{0}^T \\ -i\omega_s/\gamma & 0 & -i\omega_s/\gamma & \mathbf{0}^T \\ 0 & -i(\gamma-1)\omega_s & -\tilde{\boldsymbol{\epsilon}}_{\boldsymbol{i}}^{\mathbf{0}} \cdot \boldsymbol{\alpha} & \tilde{\boldsymbol{\epsilon}}^{\mathbf{0}} \boldsymbol{\alpha}^T \\ \mathbf{0} & \mathbf{0} & \boldsymbol{\alpha}^T & -\mathrm{diag}(\boldsymbol{\alpha}) \end{pmatrix}. \tag{44}$$

We can solve for the eigenvectors

$$\delta\tilde{v}_g = \frac{\omega}{\omega_s} \delta\tilde{\rho}_g, \tag{45}$$

$$\delta\tilde{T}_g = -\left(1 - \frac{\gamma\omega^2}{\omega_s^2}\right) \delta\tilde{\rho}_g, \tag{46}$$

$$\delta\tilde{T}_{d,i} = -\frac{\alpha_i}{\alpha_i - i\omega} \left(1 - \frac{\gamma\omega^2}{\omega_s^2}\right) \delta\tilde{\rho}_g, \tag{47}$$

$$\tag{48}$$

to obtain the following dispersion relation

$$F(\omega, \omega_s) = \omega_s^2 \left(1 + \frac{1}{\gamma} \sum_{k-1}^{N-1} \frac{\tilde{\epsilon}_k^0 \alpha_k}{\alpha_k - i\omega} \right) - \omega^2 \left(1 + \sum_{k-1}^{N-1} \frac{\tilde{\epsilon}_k^0 \alpha_k}{\alpha_k - i\omega} \right) = 0. \tag{49}$$

For a single dust species, this relation depends only on three dimensionless parameters, (1) the adiabatic index γ, (2) the relative thermal capacity of dust to gas, $\tilde{\epsilon}$, and (3) the dimensionless product ω_s/α, i.e. the ratio of the acoustic oscillation frequency to the dust cooling rate.

In the general multi-species case there $2N$ in total, for $N-1$ grain species, but if we assume a continuous power-law distribution, the effective dynamics can again be reduced to these same three controlling parameters.

To clarify the behavior of the coupled modes, we focus on the one-species case, which reveals the essential physics. Normalizing frequencies by the sound-wave scale,

$$\hat{\omega} = \frac{\omega}{\omega_s}, \qquad \hat{\alpha} = \frac{\alpha}{\omega_s}, \tag{50}$$

the dispersion relation takes the compact form

$$F(\hat{\omega}) \equiv (\gamma + S(\hat{\omega})) \; - \; \gamma\,\hat{\omega}^2 (1 + S(\hat{\omega})) = 0, \tag{51}$$

with the dust–gas coupling summarized by

$$S(\hat{\omega}) = \frac{\tilde{\epsilon}\,\hat{\alpha}}{\hat{\alpha} - i\hat{\omega}}. \tag{52}$$

Therefore we note that $S(\hat{\omega})$ modifies the effective compressibility of the medium. When dust is weakly coupled, $S \to 0$ and the waves are purely adiabatic; when dust is tightly coupled, S becomes large and the effective equation of state shifts toward isothermal. The imaginary part of S encodes cooling-induced damping. We now examine the principal asymptotic limits.

- **Gas-only limit ($\epsilon \to 0$).** In the absence of dust ($S \to 0$),

  $$\gamma\hat{\omega}^2 = \gamma \quad \Rightarrow \quad \hat{\omega} = \pm 1, \tag{53}$$

  recovering standard adiabatic sound waves.
- **Slow cooling ($\hat{\alpha} \ll 1$).** When dust exchanges heat slowly compared to the oscillation period, the dust temperature is effectively "frozen." In this regime

  $$S(\hat{\omega}) \approx i\,\tilde{\epsilon}\,\hat{\alpha}. \tag{54}$$

  For $\hat{\omega} \simeq 1$, write $\hat{\omega} = 1 + \delta$ with $|\delta| \ll 1$. Linearization yields

  $$\delta = \frac{1-\gamma}{2\gamma} S \quad \Rightarrow \quad \hat{\omega} \; \approx \; 1 \; - \; i\,\frac{\gamma - 1}{2\gamma}\,\tilde{\epsilon}\,\hat{\alpha}. \tag{55}$$

  Thus the phase speed remains essentially adiabatic, while a weak damping rate appears:

  $$-\Im\hat{\omega} \; = \; \frac{\gamma - 1}{2\gamma}\,\tilde{\epsilon}\,\hat{\alpha}. \tag{56}$$

- **Fast cooling ($\hat{\alpha} \gg 1$).** When thermal exchange is rapid compared to oscillation, gas and dust behave as a single thermodynamic fluid. Expanding,

  $$S(\hat{\omega}) \approx \tilde{\epsilon} \left(1 + i\,\frac{\hat{\omega}}{\hat{\alpha}} \right). \tag{57}$$

  To leading order $S \simeq \tilde{\epsilon}$ is real, giving

  $$\hat{\omega} \; \approx \; \pm\sqrt{\frac{\gamma + \tilde{\epsilon}}{\gamma(1 + \tilde{\epsilon})}}. \tag{58}$$

  This expression shows how the effective sound speed depends on the dust content:

- For $\tilde{\epsilon} \ll 1$,

$$\hat{\omega} \approx \pm\left[1 - \frac{\gamma - 1}{2\gamma}\,\tilde{\epsilon}\right], \tag{59}$$

  i.e. a slight reduction of the phase speed.
- For $\tilde{\epsilon} \gg 1$,

$$\hat{\omega} \to \pm\frac{1}{\sqrt{\gamma}}, \tag{60}$$

  corresponding to the isothermal sound speed.

  Damping enters only at higher order, $O(\tilde{\epsilon}/\hat{\alpha})$, reflecting that rapid cooling suppresses dissipative effects.
- **Thermal relaxation mode.** In addition to the propagating branches, there exists a purely damped mode, associated with the pole of S. Near $\hat{\omega} \simeq -i\hat{\alpha}$, write $\hat{\omega} = -i\hat{\alpha} + \delta$ with $|\delta| \ll 1$. This yields

$$\hat{\omega} \approx -i\hat{\alpha}\left(1 + \frac{\tilde{\epsilon}}{\gamma}\,\frac{1 + \gamma\hat{\alpha}^2}{1 + \hat{\alpha}^2(1 - 2\tilde{\epsilon})}\right). \tag{61}$$

  This solution corresponds not to sound propagation but to a thermal relaxation mode, in which gas and dust temperatures equilibrate on the cooling timescale $\sim \hat{\alpha}^{-1}$.

3.4. Case with thermal and momentum coupling

We now consider the more general case in which dust interacts with the gas both dynamically, through drag forces, and thermally, through collisional heat exchange. This system of coupled perturbation equations governs the linear response of the dusty fluid:

$$-i\omega\delta\tilde{\rho}_g = -i\omega_s\delta\tilde{v}_g, \tag{62}$$

$$-i\omega\delta\tilde{\rho}_{d,i} = -i\epsilon_i^0\omega_s\delta\tilde{v}_{d,i}, \tag{63}$$

$$-i\omega\delta\tilde{v}_g = -\frac{i\omega_s}{\gamma}\left(\delta\tilde{T}_g + \delta\tilde{\rho}_g\right) - \sum_{k=1}^{N-1}\frac{\epsilon_i^0}{t_{s,i}}\left(\delta\tilde{v}_g - \delta\tilde{v}_{d,i}\right), \tag{64}$$

$$-i\omega\delta\tilde{v}_{d,i} = \frac{1}{t_{s,i}}\left(\delta\tilde{v}_g - \delta\tilde{v}_{d,i}\right), \tag{65}$$

$$-i\omega\delta\tilde{T}_g = -i(\gamma - 1)\omega_s\delta\tilde{v}_g - \sum_{k=1}^{N-1}\tilde{\epsilon}_k^0\alpha_k(\delta\tilde{T}_g - \delta\tilde{T}_{d,k}), \tag{66}$$

$$-i\omega\delta\tilde{T}_{d,i} = \alpha_i(\delta\tilde{T}_g - \delta\tilde{T}_{d,i}). \tag{67}$$

This system of equations can be written in matrix form as $\mathbf{M}\tilde{\delta} = -i\omega\tilde{\delta}$, where the perturbation vector is $\tilde{\delta} = (\delta\tilde{\rho}_g, \delta\tilde{\rho}_{d,i}, \delta\tilde{v}_g, \delta\tilde{v}_{d,i}, \delta\tilde{T}_g, \delta\tilde{T}_{d,i})$ and $\mathbf{M}$ is an $(3N + 2) \times (3N + 2)$ matrix given by:

$$\mathbf{M} = \begin{pmatrix} 0 & \mathbf{0} & -i\omega_s & \mathbf{0} & 0 & \mathbf{0} \\ \mathbf{0} & \mathbf{0} & \mathbf{0} & -i\omega_s(\boldsymbol{\epsilon}^{\mathbf{0}})^T & \mathbf{0} & \mathbf{0} \\ -\frac{i\omega_s}{\gamma} & 0 & -\boldsymbol{\epsilon}^{\mathbf{0}} \cdot \boldsymbol{t_s}^{-1} & \boldsymbol{\epsilon}^{\mathbf{0}} \cdot \boldsymbol{t}_{\boldsymbol{s}}^{\mathbf{-1}} & -\frac{i\omega_s}{\gamma} & \mathbf{0} \\ \mathbf{0} & \mathbf{0} & (\boldsymbol{t_{s,i}}^{-1}) & -(\boldsymbol{t_s}^{-1})^T & \mathbf{0} & \mathbf{0} \\ 0 & \mathbf{0} & -i(\gamma - 1)\omega_s & \mathbf{0} & -\tilde{\boldsymbol{\epsilon}}^{\mathbf{0}} \cdot \boldsymbol{\alpha} & \tilde{\boldsymbol{\epsilon}}^{\mathbf{0}} \cdot \boldsymbol{\alpha} \\ \\ \mathbf{0} & \mathbf{0} & \mathbf{0} & \mathbf{0} & \boldsymbol{\alpha} & -\mathrm{diag}(\boldsymbol{\alpha}) \end{pmatrix}. \tag{68}$$

Solving for the eigenvectors, we obtain the following relations:

$$\delta\tilde{\rho}_{d,i} = \frac{\epsilon^0}{1 - i\omega t_{s,i}}\delta\tilde{\rho}_g, \tag{69}$$

$$\delta\tilde{v}_g = \frac{\omega}{\omega_s}\delta\tilde{\rho}_g, \tag{70}$$

$$\delta\tilde{v}_{d,i} = \frac{\omega}{\omega_s\,(1 - i\omega t_{s,i})}\delta\tilde{\rho}_g, \tag{71}$$

$$\delta\tilde{T}_g = (\gamma - 1)\left(1 + \sum_{k=1}^{N-1}\frac{\tilde{\epsilon}_k^0}{1 - i\omega t_{h,k}}\right)^{-1}\delta\tilde{\rho}_g, \tag{72}$$

$$= -\left(1 - \frac{\gamma\omega^2}{\omega_s^2}\left(1 + \sum_{k=1}^{N-1}\frac{\epsilon_k^0}{1 - i\omega t_{s,k}}\right)\right)\delta\tilde{\rho}_g \tag{73}$$

$$\delta\tilde{T}_{d,i} = \frac{1(\gamma - 1)}{1 - i\omega t_{h,k}}\left(1 + \sum_{k=1}^{N-1}\frac{\tilde{\epsilon}_k^0}{1 - i\omega t_{h,k}}\right)^{-1}\delta\tilde{\rho}_g, \tag{74}$$

$$= -\frac{1}{1 - i\omega t_{h,k}}\left(1 - \frac{\gamma\omega^2}{\omega_s^2}\left(1 + \sum_{k=1}^{N-1}\frac{\epsilon_k^0}{1 - i\omega t_{s,k}}\right)\right)\delta\tilde{\rho}_g. \tag{75}$$

The corresponding dispersion relation then follows as

$$F(\omega, \omega_s) = \omega_s^2\left(\gamma + \sum_{k=1}^{N-1}\frac{\tilde{\epsilon}_k^0}{1 - i\omega t_{h,k}}\right) \tag{76}$$

$$- \gamma\omega^2\left(1 + \sum_{k-1}^{N-1}\frac{\tilde{\epsilon}_k^0}{1 - i\omega t_{h,k}}\right)\left(1 + \sum_{k=1}^{N-1}\frac{\epsilon_k^0}{1 - i\omega t_{s,k}}\right) = 0. \tag{77}$$

Notably, the dispersion relation contains cross terms that depend simultaneously on the stopping time and the cooling timescale. This demonstrates that the system's dynamical and thermal responses are intrinsically coupled: energy exchange through dust–gas collisions and cooling modifies both the damping rate and the propagation speed of acoustic waves.

To assess these theoretical predictions, we compare the analytical eigenmodes with direct numerical simulations. Consistent with linear theory, the system supports two damped propagating wave solutions; we focus on one of these, as the other is simply its complex conjugate.

The simulations are initialized with a small-amplitude perturbation of the form $\delta f = A\,\tilde{\delta f}\,e^{ikx}$, with amplitude $A = 10^{-4}$ applied to velocity, density, and temperature perturbations. The unperturbed background is uniform, characterized by zero velocity, sound speed $c_s = 1$, and gas temperature $T_g = 1$. The computational domain spans $x \in [0, 1]$ with periodic boundary conditions, and we impose a perturbation wavenumber $k = 2\pi/L$ with $L = 1$.

For the coupling parameters, we adopt stopping and heating times $t_s = t_h = 0.1$, a dust-to-gas mass ratio $\epsilon = 2.24$, and an adiabatic index $\gamma = 1.4$. The dust–gas coupling coefficient is set to $c_{dg} = 0.01$, which yields an eigenfrequency for the selected mode of $-i\omega = -0.6042 - 4.1473j$. All solutions are evaluated at the spatial location x=0.

Figure 4 presents the temporal evolution of density, velocity, and internal energy perturbations in a one-dimensional setup with a single dust species. The solid curves correspond to the analytical eigenmode solutions, while the markers denote the numerical results. The close agreement across all fields confirms the predictive accuracy of the linear analysis and validates the

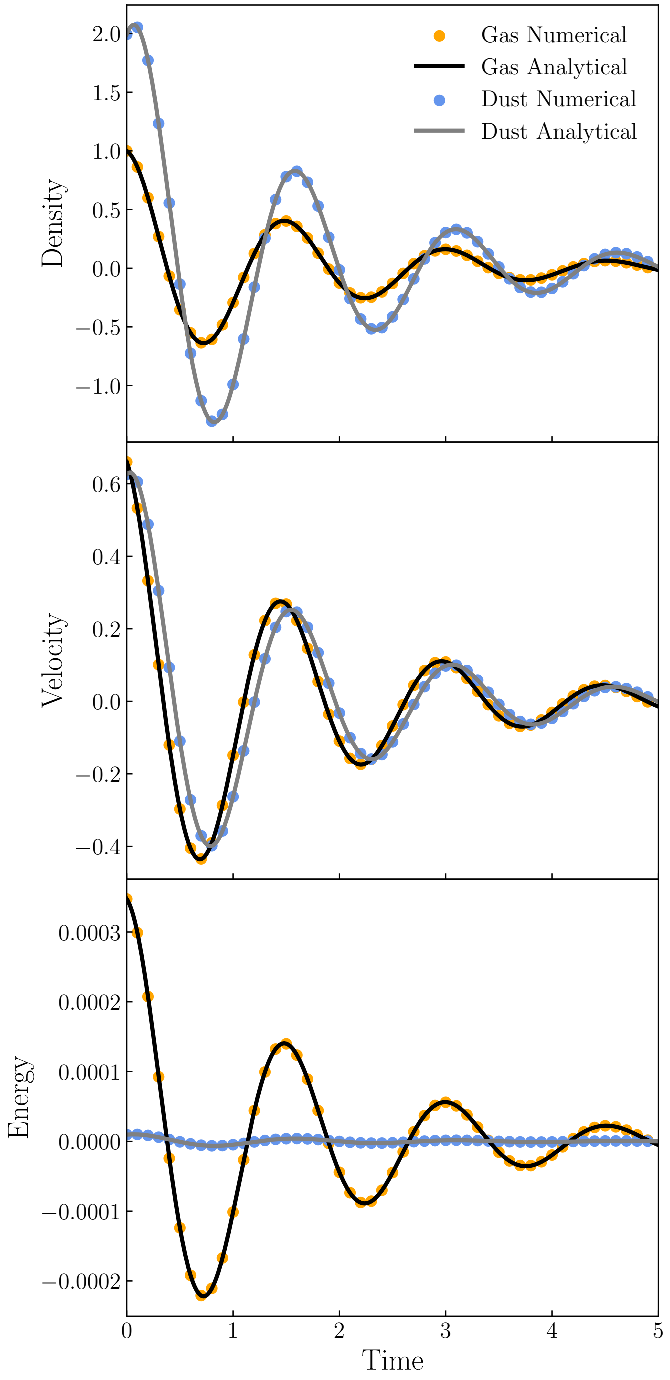

Fig. 4. Comparison of numerical (circles) and analytical (solid lines) solutions for damped sound waves with dust-gas drag and collisional heating/cooling. The plots show the perturbations in density, velocity and energy, respectively for the dust and gas components. The close match between the two validates our numerical implementation for both dust and gas components.

numerical scheme in capturing the coupled dust–gas wave dynamics.

We perform a resolution convergence test using N = 16, 32, 64, 128, 256, 512, 1024 grid cells. The numerical error is defined as Error = $\sqrt{\sum (x_{\text{sim}} - x_{\text{exact}})^2}$, where x_{sim} is the solution from the simulation and x_{exact} is the corresponding analytical solution for the gas density, velocity, and energy respectively. As shown in Figure 5, the error decreases consistently with increasing resolution, exhibiting the expected linear convergence rate. This confirms that our numerical implementation behaves correctly as the computational grid is refined.

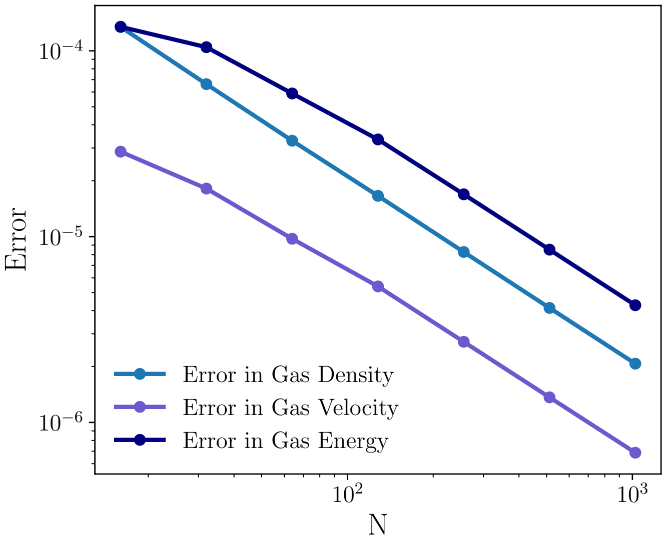

Fig. 5. Resolution convergence test showing the error in the gas density, velocity, and energy fields defined as $\sqrt{\sum (x_{\text{sim}} - x_{\text{exact}})^2}$. The error decreases linearly with increasing number of grid cells, demonstrating the expected linear convergence behavior of our numerical method.

4. Dust Radiative Cooling

So far, our analysis has considered only thermal accommodation as the mechanism coupling gas and dust temperatures. In reality, dust also cools efficiently by infrared radiation and is heated by stellar irradiation. To account for these processes, the dust energy equation must include additional terms: a radiative cooling rate that scales steeply with temperature, $\Lambda_{\text{IR}} \propto T_d^4$, and a radiative heating term from stellar irradiation that can be approximated as a constant source term.

The inclusion of radiative cooling and stellar irradiation introduces multiple characteristic timescales into the dust energy equation, leading to numerical stiffness. Physically, the dust grain temperature is regulated by the balance between heating from stellar irradiation and cooling via infrared emission. Deviations from this equilibrium, such as transient collisional heating by the gas, are rapidly damped by efficient radiative cooling, which acts to restore the dust temperature to its steady-state value.

Accurate initialization of the dust equilibrium temperature is therefore essential. We determine T_{eq} by balancing stellar irradiation absorbed by grains with their IR emission through

$$\frac{dT_d}{dt} = \Gamma_{\text{irr}} - \Lambda_{\text{IR}} = 0,$$

yielding the steady-state condition

$$T_{\text{eff}}^4 Q_{\text{irr}} = T_d^4 Q_{\text{IR}}, \tag{78}$$

$$Q_{\text{irr}} = \min\left(\frac{2\pi a}{\lambda_{\text{irr}}}, 1\right), \tag{79}$$

$$Q_{\text{IR}} = \min\left(\frac{8\pi a k_B T_d}{hc}, 1\right), \tag{80}$$

where $Q_{\rm irr}$ and $Q_{\rm IR}$ are the absorption efficiencies in the irradiation and thermal regimes, respectively. For simplicity, we neglect collisional terms and opacity effects in this initial estimate, though both can be incorporated in future radiative transfer extensions of our model.

This equilibrium admits three asymptotic regimes, depending on the ratio of the grain size to the relevant wavelengths:

$$T_{\rm eq} = \begin{cases} \left(\dfrac{hc}{4\lambda_{\rm irr} k_B}\right)^{1/4} T_{\rm eff}, & 2\pi a < \lambda_{\rm irr}, \\ \left(\dfrac{hc}{4\lambda_{\rm irr} k_B}\right)^{1/5} T_{\rm eff}^{4/5}, & \lambda_{\rm irr} \leq 2\pi a < \dfrac{hc}{4 k_B T_d}, \\ T_{\rm eff}, & \dfrac{hc}{4 k_B T_d} \leq 2\pi a, \end{cases} \tag{81}$$

with $T_{\rm eff} = T_\star (r/r_\star)^{-1/2}$. These regimes correspond to small, intermediate, and large grains, respectively.

For protoplanetary disks, the characteristic timescales for collisional and radiative cooling can be comparable over a broad range of grain sizes, and thus neither process can be neglected. We quantify these timescales as

$$t_{\rm col,d} = \left(c_d \rho_d \left|\partial \Lambda_d / \partial T_d\right|\right)^{-1}, \tag{82}$$

$$t_{\rm col,g} = \left(c_g \rho_g \left|\partial \Lambda_g / \partial T_g\right|\right)^{-1} = t_{\rm col,d}/\tilde{\epsilon}, \tag{83}$$

$$t_{\rm IR,d} = \left(c_d \rho_d \left|\partial \Gamma_{\rm IR} / \partial T_d\right|\right)^{-1}, \tag{84}$$

with

$$t_{\rm IR,d} = \frac{3\sigma_{\rm SB}}{a \rho_s c_d} \left(4 T_d^3 Q(a,T) + \frac{\partial Q}{\partial T_d} T_d^4\right)^{-1}.$$

As expected, small grains are strongly coupled to the gas and equilibrate thermally on collisional timescales much longer than their radiative cooling times. By contrast, at larger grain sizes the slope of the radiative cooling timescale changes as Q transitions from $Q \propto a/\lambda$ to $Q \approx 1$, and eventually reaches a temperature floor. Importantly, for grains between $\sim 0.1\,\mu$m and ~ 0.1 mm, the collisional and radiative timescales are comparable, implying that both processes must be included to accurately capture dust–gas thermodynamics. This is illustrated in Figure 6.

In practice, the radiative cooling term can be incorporated via operator splitting, where the dust radiative losses are advanced separately using an effective cooling time. This approach provides numerical stability while retaining the correct physical scaling across grain sizes.

4.1. Implicit Solver Including Dust Thermal Accommodation and Radiative Cooling

Another approach to modeling the thermal interaction between gas and dust, while accounting for dust radiative cooling is to solve the coupled energy equations for both phases simultaneously using a fully implicit scheme. By incorporating both collisional energy exchange and radiative losses into a single step, this method enables stable and efficient evolution of the system, even in the presence of stiff source terms where cooling timescales become much shorter than the hydrodynamic timestep. We begin with the energy equations governing the gas and each dust species:

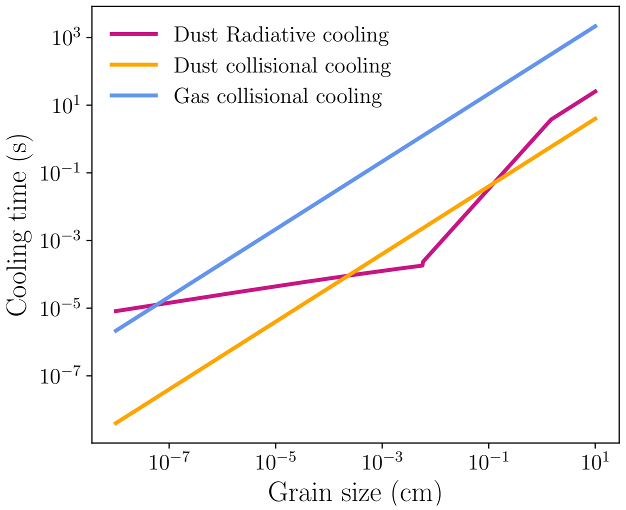

Fig. 6. Cooling timescales as a function of grain size for $\epsilon = 0.01$, $c_{dg} = 0.088$, and typical mid-plane disk densities of $\rho_g \sim 10^{-13}$ g cm^{-3}. Initial conditions assume the smallest grains at $T = 10$ K, with larger grains following radiative equilibrium down to a temperature floor of 2.5 K.

$$\rho_g c_{v,g} \frac{dT_g}{dt} = -\Lambda_g, \tag{85}$$

$$\rho_{d,i} c_{v,d} \frac{dT_{d,i}}{dt} = \Lambda_{d,i} - \Gamma_{d,i}, \tag{86}$$

$$\Lambda_g = \sum_{k=1}^{N-1} \Lambda_{d,k}, \tag{87}$$

$$\Lambda_{d,i} = \pi a_{d,i}^2 n(a_{d,i}) n_g \bar{v} g(2\mathcal{A}) k_B (T_g - Td,i), \tag{88}$$

$$\Gamma_{d,i} = 4\pi a_{d,i}^2 n(a_{d,i}) Q(a_{d,i}, T_{d,i}) \sigma_{\rm SB} \left(T_{d,i}^4 - T_{{\rm eq},i}^4\right). \tag{89}$$

We define the characteristic coefficients

$$\alpha_i = \frac{3(k_B/\bar{m})^{3/2} T_g^{1/2} \rho_g}{4 \rho_s c_{v,d} a_i}, \tag{90}$$

$$\beta_i = \frac{12 \sigma_{\rm SB} Q T_{d,i}^3}{\rho_s a_i}, \tag{91}$$

which represent the dust–gas thermal coupling and radiative cooling rates, respectively.

Discretizing the system over a timestep Δt yields a set of coupled linear equations for the gas and dust temperatures at time t^{n+1}:

$$\begin{cases} \left(1 + c_{dg} \sum\limits_{k=1}^{N-1} \epsilon_k^n \alpha_k^n \Delta t\right) T_g^{n+1} - c_{dg} \sum\limits_{k=1}^{N-1} \epsilon_k^n \alpha_k^n \Delta t, T_{d,k}^{n+1} = T_g^n, \\ -\alpha_i^n \Delta t, T_g^{n+1} + \left(1 + (\alpha_i^n + \beta_i^n)\Delta t\right) T_{d,i}^{n+1} - \beta_i^n \Delta t, T_{{\rm eq},i} = T_{d,i}^n, \quad \forall i. \end{cases} \tag{92}$$

Solving this system yields closed-form expressions for the updated temperatures:

$$T_g^{n+1} = \frac{p^n}{\rho^n}, \tag{93}$$

$$T_{d,i}^{n+1} = \frac{T_{d,i}^n + \beta_i^n \Delta t, T_{{\rm eq},i} + \alpha_i^n \Delta t, (p^n/\rho^n)}{1 + (\alpha_i^n + \beta_i^n)\Delta t}, \tag{94}$$

where we define effective pressure and density terms:

$$p^n = \rho_g^n T_g^n + c_{dg} \sum_{k=1}^{N-1} \frac{\alpha_k^n \Delta t}{1 + (\alpha_k^n + \beta_k^n)\Delta t} \rho_{d,k}^n T_{d,k}^n, \tag{95}$$

$$\rho^n = \rho_g^n + c_{dg} \sum_{k=1}^{N-1} \frac{\alpha_k^n \Delta t}{1 + (\alpha_k^n + \beta_k^n)\Delta t} \rho_{d,k}^n. \tag{96}$$

It is straightforward to show that in the limit where both $\alpha\Delta t \ll 1$ and $\beta\Delta t \ll 1$, the effective thermal relaxation rate defined by

$$\alpha_{\mathrm{eff}} = \frac{1}{\Delta t} \log\left(\frac{T_g^{n+1} - T_d^{n+1}}{T_g^n - T_d^n} \right) \tag{97}$$

reduces to the correct effective rate$\alpha_{\mathrm{eff}} \rightarrow \tilde{\epsilon}\alpha$. However, this limit does not always apply in practice. In realistic systems, some dust species may have radiative cooling timescales that are extremely short compared to the timestep ($\beta\Delta t \gg 1$), while still being weakly coupled to the gas ($\alpha\Delta t \ll 1$). In such cases, we find that it is not necessary to resolve the dust cooling timescale in order to accurately capture the gas thermal evolution.

Specifically, we find that the gas temperature is insensitive to whether$\beta\Delta t$ is resolved, provided that $\alpha\Delta t$ is. Since the gas energetics are the primary driver of thermal instabilities and dynamics, this is advantageous as it implies that even if the dust rapidly cools and its temperature is not time-resolved, the gas cooling is still computed accurately. The dust, being tightly bound to its radiative equilibrium, quickly equilibrates within a timestep and simply acts as a heat sink for the gas.

In the asymptotic regime where $\beta\Delta t \gg 1$ and $\alpha\Delta t \ll 1$, the dust temperature relaxes to equilibrium ($T_d^{n+1} \rightarrow T_{\mathrm{eq}}$) on a timescale much shorter than the timestep. Substituting into the gas equation, we recover the expected two-temperature solution:

$$T_g^{n+1} = \frac{T_g^n + \tilde{\epsilon}\,\alpha\Delta t\, T_{\mathrm{eq}}}{1 + \tilde{\epsilon}\,\alpha\Delta t}, \tag{98}$$

with an effective gas cooling rate $\alpha_{\mathrm{eff}} \approx \tilde{\epsilon}\alpha$. This confirms that our method correctly retrieves the gas thermodynamics even in the limit of stiff dust cooling.

This behavior highlights a key advantage of the implicit approach. Explicit schemes are limited by stability constraints that require timesteps small enough to resolve the fastest cooling process, in this case, radiative losses with timescale β^{-1}. When $\beta\Delta t \gg 1$, explicit methods become unstable and unable to capture the correct evolution, effectively excluding this regime from practical simulation. In contrast, the implicit method remains stable regardless of β, allowing accurate integration across a much wider range of cooling rates. This relaxes the timestep constraint by a factor of β/α, which can be orders of magnitude for small grains with rapid radiative cooling.

The generality of this approach becomes particularly important when a grain size distribution is present. Because both α_i and β_i depend on grain size, different dust species will naturally occupy different thermal regime, some cooling rapidly, others more slowly, some tightly coupled to the gas, others thermally independent. A formulation that can consistently transition between these limits without modification is therefore essential for physical fidelity. It ensures that the correct gas temperature evolution is captured regardless of the dust regime, while also enabling the treatment of mixtures of grains spanning a wide parameter space.

5. VSI Simulations

We now apply our non-equilibrium thermodynamics framework to hydrodynamic simulations of the VSI in protoplanetary disks. Our primary goal is to assess how realistic, grain-mediated cooling processes influence the onset and growth of the instability. In particular, we focus on the interplay between collisional energy exchange and a physically motivated dust population, which together regulate the thermal relaxation timescale. This approach extends previous VSI studies, which often employed simplified prescriptions such as locally isothermal or fixed β-cooling models, by explicitly incorporating dust–gas thermal coupling.

As a first test case, we consider a monodisperse dust distribution with grain size $a = 10^{-5}$ cm embedded in a representative disk model at 30 AU. The disk is initialized with a surface density slope of $p = 3.5$, a dust-to-gas mass ratio of $\epsilon = 0.01$, and a dust–gas coupling parameter of $c_{dg} = 0.1$. We note that under these conditions, the cooling is sufficiently efficient to allow the VSI to grow throughout the disk, thereby recovering the isothermal solution.

Hoever, we also note that Under these conditions, the cooling timescale associated with dust–gas collisions is comparable to the hydrodynamic timestep. This stiffness poses a numerical challenge: advancing the system with a single Courant-limited timestep leads to inaccurate thermal relaxation. To mitigate this issue, we implement subcycling for the thermal energy update, allowing the dust and gas temperatures to evolve with a timestep smaller than that used for the hydrodynamics.

We find that subcycling of the thermal cooling terms is essential for achieving numerical convergence. In Figure 7, we compare simulations with different numbers of thermal substeps (0, 10, and 50) against fully isothermal reference runs. The simulations are performed in two dimensions at a resolution of 512^2 cells. Without subcycling, the vertical shear instability is artificially suppressed, yielding damped vertical motions. Increasing the number of thermal substeps progressively restores agreement with the expected isothermal growth rates. However, even with 30 substeps, the growth remains under-resolved, indicating that additional refinement is necessary.

A key next step is to quantify the number of substeps required for full convergence and to assess whether this strategy provides a robust and computationally efficient approach for coupling dust–gas thermodynamics in global VSI simulations.

6. Conclusions

In this work, we have developed and applied a non-equilibrium thermodynamic framework for modeling dust–gas thermal coupling in protoplanetary disks, with a particular focus on its implications for the VSI. Our formulation captures both collisional energy exchange and radiative cooling of dust grains, and can accommodate a physically motivated grain size distribution spanning a wide range of cooling regimes. Our main conclusions are as follows:

1. **Implicit collisional and radiative cooling.** The method allows stable integration of dust and gas temperatures across a wide range of cooling regimes. Unlike explicit approaches, which require $\Delta t \lesssim 1/\min(\beta_i, \alpha_i)$ to follow the fastest dust cooling rates, the implicit method only requires $\Delta t \lesssim 1/\alpha_i$ to recover the correct gas thermal evolution.
2. **Two-fluid thermal relaxation and wave propagation tests.** We validated the method against a suite of problems, including dust–gas thermal relaxation and the propagation of

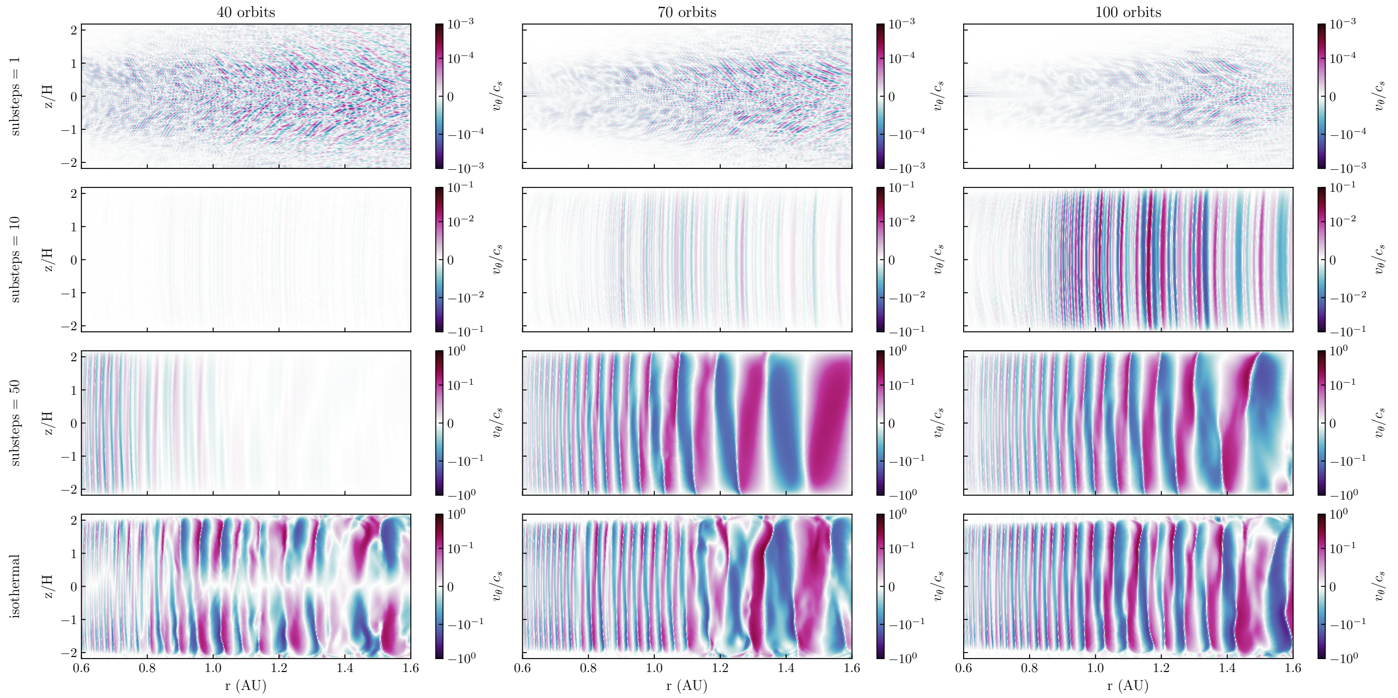

Fig. 7. Vertical velocity fields at 40, 70, and 100 orbits for VSI simulations including dust–gas thermal coupling. Each set of panels shows results with different numbers of thermal substeps (0, 10, and 50), compared against a fully isothermal reference run shown at the bottom. The simulations are two-dimensional with a resolution of 512^2 cells. Subcycling the thermal update is necessary to recover the correct VSI growth rate and avoid artificial damping of vertical motions.

damped sound waves. The dispersion relation analysis shows that both the sound speed and damping rate depend sensitively on the degree of thermal accommodation between gas and dust. In the stiff regime, the implicit method remains unconditionally stable, but accuracy requires that the effective gas cooling time be resolved; otherwise, the cooling rate is underestimated.

3. **Application to the VSI.** We applied the method to simulations of the Vertical Shear Instability in protoplanetary disks, with realistic dust-mediated cooling. We showed that convergence requires subcycling of the thermal equations: by integrating the dust and gas temperatures on substeps, we recover the correct gas cooling without reducing the global hydrodynamic timestep. This allows VSI growth to be captured efficiently while resolving the relevant thermodynamics.

Overall, our results establish that implicit methods for dust–gas collisional and radiative cooling can efficiently capture the full range of dust thermal physics while maintaining accuracy in the gas. By recovering the correct dispersion properties of sound waves and the correct cooling rates in disk instabilities, this framework provides a foundation for studying turbulence, wave propagation, and dust–gas thermodynamics in protoplanetary disks across a broad range of grain sizes and cooling regimes.

Acknowledgements. This work originated from a project of the Summer Program in Astrophysics 2025 held at the University of Virginia, and funded by the Center for Global Inquiry and Innovation, the National Science Foundation (Grant 2452494), the National Radio Astronomy Observatory (NRAO), the Kavli Foundation and the Heising-Simons Foundation.

References

Armitage, P. J. 2011, Annual Review of Astronomy and Astrophysics, 49, 195
Barker, A. J. & Latter, H. N. 2015, Monthly Notices of the Royal Astronomical Society, 450, 21
Barranco, J. A., Pei, S., & Marcus, P. S. 2018, The Astrophysical Journal, 869, 127
Benítez-Llambay, P., Krapp, L., & Pessah, M. E. 2019, The Astrophysical Journal Supplement Series, 241, 25
Benítez-Llambay, P. & Masset, F. S. 2016, The Astrophysical Journal Supplement Series, 223, 11
Birnstiel, T., Klahr, H., & Ercolano, B. 2012, Astronomy & Astrophysics, 539, A148
Burke, J. R. & Hollenbach, D. 1983, Astrophysical Journal, Part 1, vol. 265, Feb. 1, 1983, p. 223-234., 265, 223
Chiang, E. & Goldreich, P. 1997, The Astrophysical Journal, 490, 368
Chiang, E. & Youdin, A. 2010, Annual Review of Earth and Planetary Sciences, 38, 493
Draine, B. T. 2011, Physics of the interstellar and intergalactic medium, Vol. 19 (Princeton University Press)
Goldreich, P. & Schubert, G. 1967, ApJ, 150, 571
Lesur, G., Flock, M., Ercolano, B., et al. 2023, in Astronomical Society of the Pacific Conference Series, Vol. 534, Protostars and Planets VII, ed. S. Inutsuka, Y. Aikawa, T. Muto, K. Tomida, & M. Tamura, 465
Lin, M.-K. & Youdin, A. N. 2015, The Astrophysical Journal, 811, 17
Lyra, W. & Umurhan, O. M. 2019, Publications of the Astronomical Society of the Pacific, 131, 072001
Malygin, M., Klahr, H., Semenov, D., Henning, T., & Dullemond, C. 2017, Astronomy & Astrophysics, 605, A30
Manger, N., Pfeil, T., & Klahr, H. 2021, Monthly Notices of the Royal Astronomical Society, 508, 5402
Nelson, R. P., Gressel, O., & Umurhan, O. M. 2013, Monthly Notices of the Royal Astronomical Society, 435, 2610
Pfeil, T. & Klahr, H. 2021, The Astrophysical Journal, 915, 130
Stoll, M. H. & Kley, W. 2014, Astronomy & Astrophysics, 572, A77
Thi, W., Lesur, G., Woitke, P., et al. 2019, Astronomy & Astrophysics, 632, A44
Urpin, V. 2003, Astronomy & Astrophysics, 404, 397
Urpin, V. & Brandenburg, A. 1998, Monthly Notices of the Royal Astronomical Society, 294, 399
Youdin, A. N. & Lithwick, Y. 2007, icarus, 192, 588